THE JOURNAL OF PHYSICAL CHEMISTRY LETTERS
A JOURNAL OF THE AMERICAN CHEMICAL SOCIETY

pubs.acs.org/JPCL

Letter

Enhancement of Photocatalytic and Photoelectrochemical Performance of ZnO by Mg Doping: Experimental and Density Functional Theory Insights

Abinash Das, Dongyu Liu, Riu Riu Wary, Andrey S. Vasenko, Oleg V. Prezhdo,* and Ranjith G. Nair*

Cite This: *J. Phys. Chem. Lett.* 2023, 14, 4134–4141

Read Online

ACCESS | Metrics & More | Article Recommendations | Supporting Information

ABSTRACT: Doped ZnO nanostructures have shown great potential for solar energy applications. Considering the compatible ionic radius, Mg atoms can be doped into ZnO at different concentrations. The current work reports a combined experimental and density functional theory study on the influence of the Mg dopant concentration on ZnO performance simultaneously for photocatalytic dye removal and photoelectrochemical water splitting. Among all the samples, Mg(3)-ZnO (3 at. % Mg) exhibits superior sunlight-driven photocatalytic performance. The optimal Mg-ZnO shows an 8-fold increase in the photocatalytic activity compared to the pristine ZnO. Likewise, the most active photocatalyst shows high photoelectrochemical performance with a photocurrent response of 1.54 mA at the lowest onset potential, 11 times higher than the pristine ZnO. Tuning of the Mg content results in the generation of extra charge carriers and a reduced recombination rate, which are the crucial factors responsible for enhanced photocatalytic and photoelectrochemical performance.

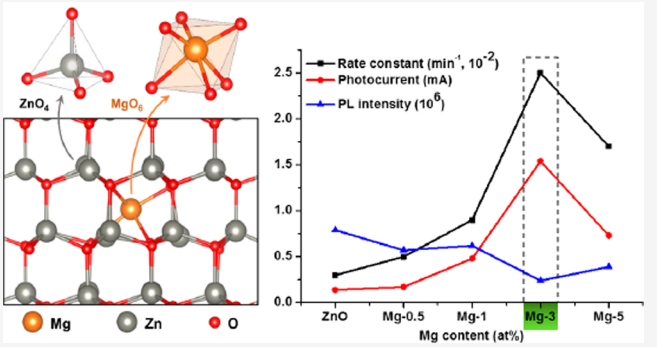

In recent years, photocatalytic removal of organic compounds in wastewater using solar energy and splitting of water in a photoelectrochemical (PEC) cell have been considered as potentially sustainable approaches for water decontamination and energy generation.[1,2] However, the development of efficient photoactive materials is a major challenge for both of these applications. In recent times, zinc oxide (ZnO) has emerged as a stable photoactive material with a direct bandgap of 3.37 eV.[3] Considering its various advantages, ZnO is considered a suitable choice for photocatalysis or PEC applications. Thus, the development of stable and efficient catalysts for achieving a high dye degradation rate and photoconversion efficiency (PCE) is highly desirable.[4−6] However, the performance of ZnO is limited due to its poor optical response and rapid recombination of photoinduced charge carriers.[7] These limitations can be addressed by employing different strategies, such as coupling of semiconductors, incorporation of cationic/anionic dopants, and sensitization.[8−10] Researchers have succeeded in the synthesis of substitutional doping of ZnO with elements such as Cu, P, Mn, and Mg, which can promote the formation of interband states and charge carrier generation.[11−13] In order to modulate the optical properties and tune the surface activity, the hybridization of ZnO with a suitable dopant is very crucial. This can assist the generation and transportation of charge carriers to catalyst surface for participating in photocatalytic and water splitting reactions.[14] Mg^{2+} (0.57 Å) ion with comparable ionic radii of the Zn^{2+} (0.60 Å) ion can replace the Zn atom in the lattice and hence is considered to be a suitable dopant element.[15] Although many reports are available on the photocatalytic dye removal application of Mg-doped ZnO nanostructures, their use in PEC water splitting is rare, while dual applications of Mg-doped ZnO have yet to be reported. The solubility of Mg ions in zinc oxide is limited and depends on the deposition technique, along with process conditions. However, Mg atoms beyond a certain percentage lead to the formation of MgO (~7.5 eV), which widens the bandgap in the UV region.[16,17] Therefore, tuning the doping concentration is vital to ensure the optimum substitution of Mg into the ZnO lattice, which can boost the optical and physicochemical properties of the material. In addition, Mg-doped ZnO is commonly prepared under a high-temperature treatment. Besides the energy waste, this characteristically leads to the formation of wide-bandgap materials with low surface areas due to the accumulation and damage to pore structures.[18,19] Hence, the preparation of doped ZnO at low temperatures is highly preferred. On the other hand, the optical and electronic

Received: March 19, 2023
Accepted: April 24, 2023
Published: April 27, 2023

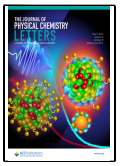

https://doi.org/10.1021/acs.jpclett.3c00736
J. Phys. Chem. Lett. 2023, 14, 4134–4141

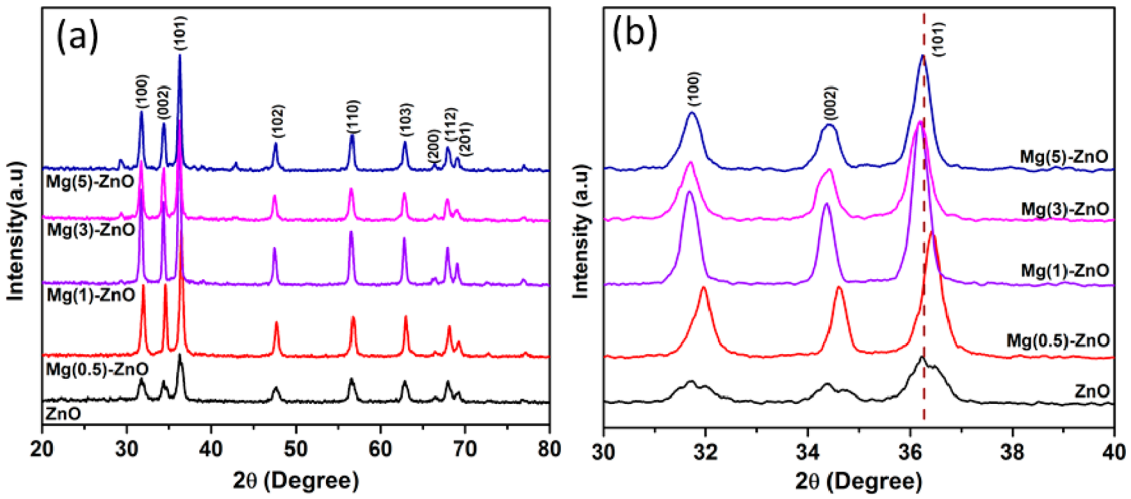

Figure 1. (a) XRD spectra and (b) peak shifts of the samples.

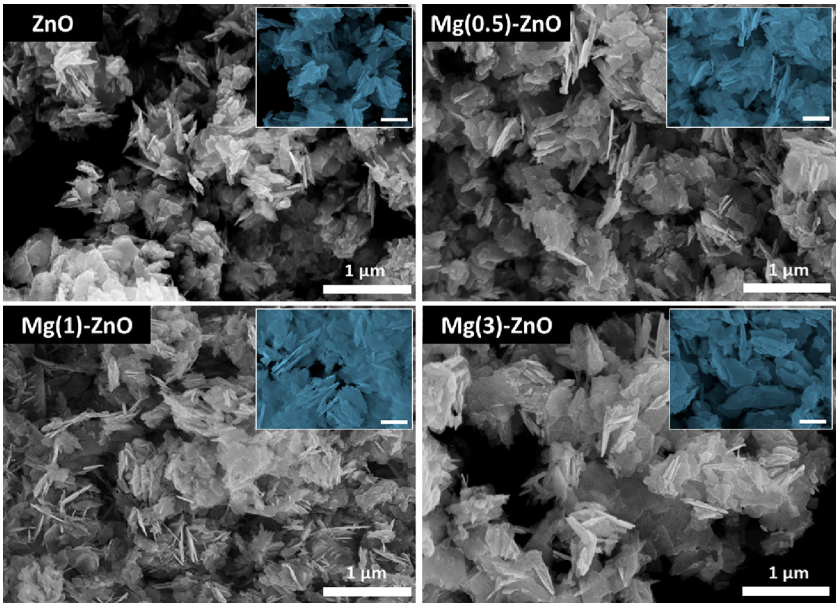

Figure 2. FESEM image of the samples. The insets of the images show accumulation of flake-like structures. The corresponding scale bar is 500 nm.

properties of the material are essential in interpreting photocatalytic dye degradation and water splitting processes. Thus, it is necessary to obtain a broad idea about the role of Mg doping on the band structure through a comparative theoretical study using density functional theory (DFT) calculations and experimental outcomes.

Based on the above consideration, the current work demonstrates the role of Mg doping in enhanced photocatalytic and PEC performance. The performance of ZnO is tuned by changing the doping percentage of Mg inside the ZnO lattice. Various physicochemical properties of modified ZnO are studied to confirm the performance and characterize the system. The correlation of the performance of the doped material with the optical properties and its positive impact are discussed based on the basis of DFT calculations and detailed material characterizations.

Zinc nitrate hexahydrate ($Zn(NO_3)_2{\cdot}6H_2O$), magnesium nitrate hexahydrate ($Mg(NO_3)_2.6H_2O$), and sodium hydroxide (NaOH) were purchased from Merck (India) and used as the precursor. Millipore distilled water was used as the solvent during the course of the sample preparation process. For the preparation of Mg-doped ZnO at different dopant percent (0.5, 1.0, 3.0, and 5.0 at. %), zinc nitrate and manganese nitrate hexahydrate of desired amount were dissolved in 100 mL of distilled water and kept in a magnetic stirrer for 5 min. A separate 1 M concentration of sodium hydroxide was prepared and added dropwise in the initial solution to make pH = 10. After constant stirring for 2 h at room temperature, a white gelatinous precipitate was formed. The white precipitate was filtered and washed with distilled water and ethanol many times to remove the impurities. The final precipitate was dried in an oven at 150 °C for 12 h. The dried precipitates were ground and calcined at 400 °C with 4 °C min^{-1} ramping rate for 1 h in a muffle furnace. Depending upon the Mg content (Mg: 0.5, 1, 3, and 5 at. %) in ZnO, the samples are labeled as Mg(0.5)-ZnO, Mg(1)-ZnO, Mg(3)-ZnO, and Mg(5)-ZnO, respectively. Details of the characterization techniques, photocatalytic experiment, and linear sweep voltammogram (LSV) experiment were provided in the Supporting Information.

https://doi.org/10.1021/acs.jpclett.3c00736
J. Phys. Chem. Lett. 2023, 14, 4134−4141

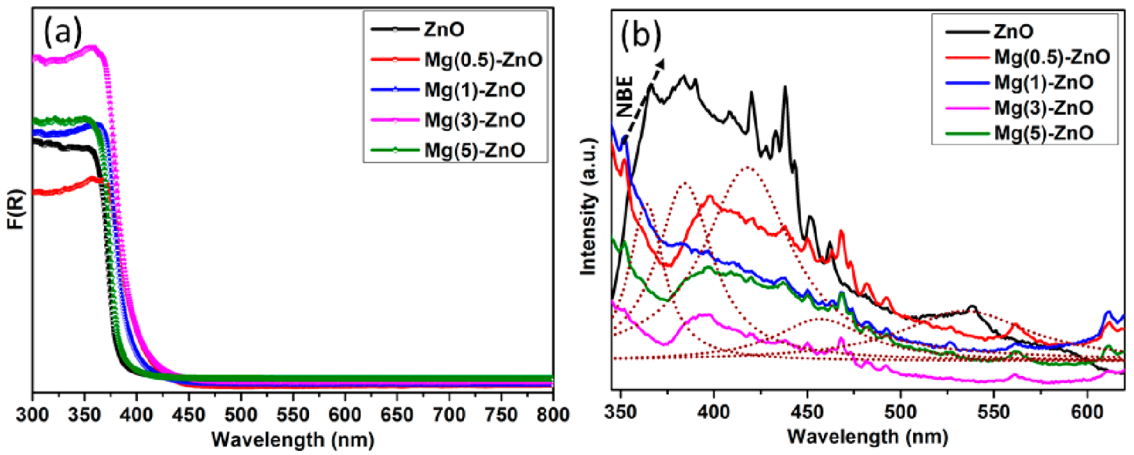

Figure 3. (a) UV−vis DRS spectra and (b) PL spectra of the samples.

All DFT calculations were performed with the QUANTUM ESPRESSO software package.[20,21] The Perdew−Burke−Ernzerhoff (PBE) functional[22] was used for geometry optimization, and the PBE0 hybrid functional[23] was used for the electronic structure calculations. A plane wave basis in conjugation with the optimized norm-conserving Vanderbilt pseudopotentials[24] was adopted. The plane wave cutoff energies for the wave function and charge density calculations were set to 80 and 320 Ry, respectively. The ZnO bulk was represented by a 3 × 3 × 2 supercell containing 72 atoms. An Mg atom was introduced at the cavity site to construct the interstitial dopant. The Brillouin zone was sampled with a 2 × 2 × 2 *k*-point mesh. The structures were visualized by using the VESTA software package.[25]

The X-ray diffraction (XRD) pattern of the samples was recorded to identify the crystallite phase of pure and Mg-doped ZnO nanostructures, as shown in Figure 1a. All the diffraction peaks of Mg-doped samples below 5 at. % correspond to the pure wurtzite phase of ZnO and are in agreement with JCPDS file No. 36-1451. No additional crystalline phase was detected up to the optimal doping limit (3 at. %), which indicates the successful doping of Mg atoms in the ZnO lattice due to their identical ionic radii. The introduction of magnesium as a dopant slightly shifts the diffraction peaks, signifying the contraction of the unit cell to host the foreign atom.[26] However, the XRD peaks of the samples beyond 1 at% doping showed a minor shift toward lower 2θ angle as shown in Figure 1b, which is probably due to the formation of doping-induced crystal defects in ZnO.[27] On the other hand, doping ratios beyond 3 at. % result in the formation of an additional peak, which can be attributed to the formation of the MgO phase.[28] The crystalline size of the samples is calculated using the Debye-Scherrer formula.[29] Among all of the doped samples, Mg(3)-ZnO with optimal doping exhibits a smaller crystalline size, indicating an expansion of the unit cell, most likely due to the presence of Mg atoms in the interstitial sites. This result demonstrates that the optimal doping content can have a desired effect on the crystallinity of the material, while excess doping may produce additional impurities without reaching the desired location in the ZnO lattice.

The field-emission scanning electron microscopy (FESEM) image in Figure 2 shows that the undoped and Mg-doped ZnO are composed of inhomogeneous nano- to microsized flakes with diameters in the range of 80−400 nm. Importantly, the inclusion of Mg dopant did not alter the morphology of the samples significantly, while the mean diameter of the flakes seemed to increase with an increase in Mg content. Therefore, it can be deduced that the surface morphology of Mg-modified ZnO remains almost unchanged, which is similar to previous reports,[30] where doping of ZnO could result in a minimal impact on the overall morphology compared to the pristine one. Furthermore, ZnO has different surface energies along different plane directions, and their growth rate in a certain direction determines the morphology of the material. Whenever the growth of ZnO along the (0002) plane is higher, it results in the formation of one-dimensional (1D) nanostructures.[31] The diffraction intensities in XRD spectra (See Figure 1) show that the ratio of (0002) and the (10−10) in doped and undoped ZnO is less than 1. Due to this anisotropic growth, the ratio becomes 0.84, 0.98, 0.94, 0.96, and 0.95 for ZnO, Mg(0.5)-ZnO, Mg(1)-ZnO, Mg(3)-ZnO, and Mg(5)-ZnO, respectively, which correlates well with the flakes like flat morphology of the samples. This could be due to the suppression of growth along the (0002) plane relative to the (10−10) plane and most likely assists the lateral growth of ZnO compared to axial growth, as is apparent from the FESEM images.[32]

Energy-dispersive X-ray spectroscopy (EDS) mapping in Figure S1 reveals the presence of Zn, Mg, and O elements in the doped samples without the presence of other contaminant elements. EDS spectra for Mg-doped ZnO with 0.5, 1.0, and 3.0 atomic percentages of Mg show that the peaks correspond to the aforementioned O, Mg, and Zn elements. The corresponding atomic percentages of the elements are depicted in the table in Figure S1, which is consistent with the stoichiometry of Mg-doped ZnO. Furthermore, EDS analysis reveals that samples doped up to 3 at. % contain Zn, O, and Mg and, when combined with XRD analysis, which shows no diffraction peaks of MgO (aside from 5 at. % of Mg), confirms Mg elements are successfully substituted inside ZnO up to the optimal limit, since the solubility of Mg in ZnO is limited, and alternatively, XRD could not detect any diffraction peaks up to 3 at. % of Mg due to the presence of Mg in small quantities. Thus, compositional and structural analyses using EDS and XRD are in good agreement, indicating an optimal doping limit (3 at. %) of Mg in the ZnO lattice.

Figure 3a displays the optical response of undoped and Mg-doped ZnO nanostructures using UV−vis absorption spectra. It is clearly indicated that ZnO exhibits an excitonic absorption edge near 390 nm, which is characteristic of ZnO.[33] The Mg

https://doi.org/10.1021/acs.jpclett.3c00736
J. Phys. Chem. Lett. 2023, 14, 4134−4141

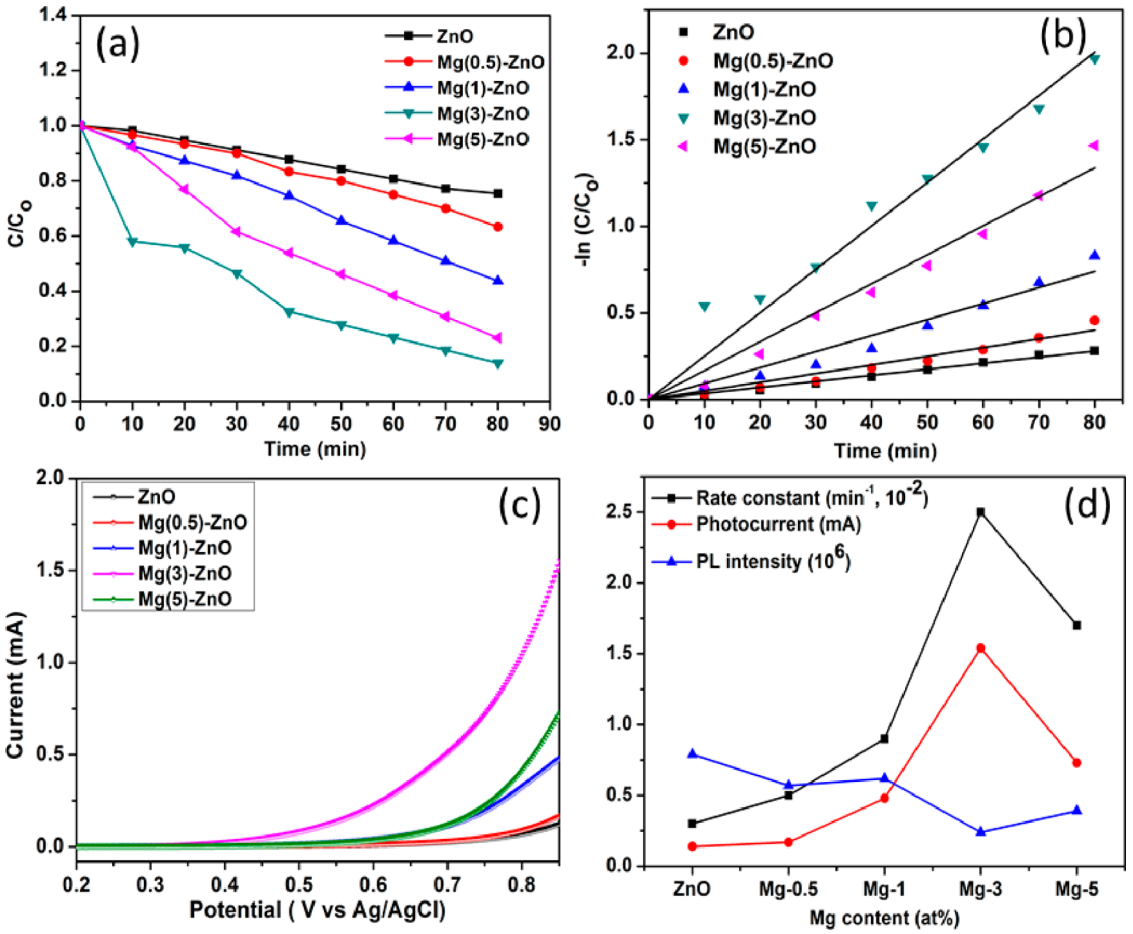

Figure 4. (a, b) Kinetics of photocatalytic degradation of MB using undoped and Mg-doped ZnO. (c) LSVs of the samples. (d) Comparisons of rate constant, photocurrent response, and PL intensity of the samples.

doping has a very minimal effect on the optical response of ZnO and results in a slight shift in the cutoff wavelength. This shift is proportional to the doping content of Mg present in ZnO, and the optimal content is found for Mg(3)-ZnO. This can be due to the introduction of defects after the substitution of Mg atoms inside the ZnO lattice, which is influenced by the difference in the electronegativity and ionic radii. ZnO is an n-type semiconductor with the Fermi level located well inside the conduction band, and as a result of Mg doping, more electrons are contributed from the lower electron affinity level of MgO compared to ZnO.[27,34] As a result, the Fermi level of Mg-doped ZnO is most likely to yield the radiative recombination of excitons, and consequently, the absorption characteristic of the doped ZnO remains almost unaltered. A slight redshift in the absorption edge of doped ZnO is observed up to the optimal doping limit, which could be attributed to the incorporation of Mg into the ZnO crystal lattice under the low-temperature synthesis method and is in good agreement with the reported result.[35] In order to obtain deeper insight about the optical and electronic properties of modified ZnO, a DFT study was also conducted and is discussed in the later section.

Room-temperature photoluminescence (PL) spectra of pristine and Mg-doped ZnO are shown in Figure 3b. The PL spectra of the samples were measured at wavelengths ranging from the ultraviolet (UV) to the visible region with an excitation wavelength of 320 nm. A sharp peak originating from the near-band emission (NBE) of pure and doped ZnO was observed in the UV region.[36] The peak corresponds to the NBE emission of Mg-doped ZnO and showed a blueshift to a lower wavelength region compared to pure ZnO. As the doping concentration increases, the shift in the NBE emission peak increases. The blueshift of the NBE peak in the PL study shed light on the absorption data and was believed to originate from the well-known Moss-Burstein effect, caused by the generation of excess electrons due to the oxygen vacancies after the substitution of Mg^{2+}.[37,38] The increase in oxygen vacancies and electron concentrations is attributed to the difference in electronegativity and ionic radius between Zn and Mg. Consequently, the states below the conduction band of ZnO are filled, and as a result, the absorption edge shifts to the higher energy level via the Burstein−Moss shift to counter the occupied states close to the conduction band. The results show that, as Mg doping increases, the shift of the NBE also increases, reaches a maximum when Mg is 3 at. %, and decreases thereafter. This is due to the modulation of the absorption capacity of ZnO caused by Mg substitution, which suggests that the optical response of the Mg-doped ZnO can be tuned by adjusting the Mg content inside the ZnO nanostructure.[39] The extent of the blueshift of the NBE peak in the doped samples is slightly different than that of the absorption edge widening, possibly caused due to the Stokes shift, often referred to as the difference of emission peak and bandgap energy.[19,40] Apart from NBE, samples exhibit a broad emission peak in the visible region around 420−570 nm. Unlike undoped ZnO, few additional PL emission peaks found

https://doi.org/10.1021/acs.jpclett.3c00736
J. Phys. Chem. Lett. 2023, 14, 4134−4141

for Mg-doped ZnO around 470 nm correspond to the green region of the visible spectrum and can be attributed to the transition between excited optical centers and the deep level of the valence band.[41] Such emission often originates from the presence of mid band structural defects formed through the suitable tuning of defect states. Another emission in the 420−490 nm range often originates due to the transition of zinc interstitial and zinc vacancy states.[42] The broad peak around 550 nm is assigned to the transition between the oxygen vacancy and valence bands.[42,43] Furthermore, it is a well-known fact that PL emission originates from the recombination of photogenerated charge carriers and the corresponding intensity provides information regarding the kinetics of recombination. The strong correlation between photocatalytic activity and PL intensity has previously been reported, and low PL emission intensities were found to be suitable for the efficient photocatalyst.[27,44] In this study, it has been observed that Mg(3)-ZnO with optimal Mg loading exhibits the lowest PL intensities compared to the remaining undoped and doped ZnO, which represents successful separation of photoinduced charge carries. Mg(3)-ZnO, in contrast to other samples, is expected to show superior photocatalytic and water splitting performance due to the low recombination rate of the electron−hole pair induced by the optimal amount of Mg in the ZnO lattice. On the other hand, Mg(5)-ZnO with maximum Mg concentration leads to the formation of the MgO secondary phase (as seen in Figure 1a), which may act as electron−hole recombination centers, and as a result Mg(5)-ZnO exhibits an increment in PL intensity compared to the optimally designed Mg(3)-ZnO.

The sunlight-driven photocatalytic performance of the samples was investigated using methylene blue (MB) as a probe pollutant and interpreted from the corresponding degradation kinetics obtained from the L-H model as shown in Figure 4a,b.[44,45] The kinetics of the photocatalytic activity reveal that the Mg-doped ZnO at different doping ratios exhibited improved performance in comparison to the pristine ZnO. Interestingly, the photocatalytic performance of the samples was found to be a function of the Mg content in ZnO (see Table 1), and with an increase in Mg concentration there is a linear increment in the photocatalytic performance. This substantiates the role of Mg doping content in improving photocatalytic performance. Moreover, as anticipated from the optical analyses, Mg(3)-ZnO with optimal Mg content (3 at%) outperforms other samples in terms of rate constant and photonic efficiency, which can be attributed to the reduced charge carrier recombination rate aided by the suitable defect states of the sample, whereas further increases in the Mg content caused a drastic reduction in the photocatalytic performance, and thus Mg(5)-ZnO showed low activity compared to Mg(3)-ZnO. The most photoactive sample, Mg(3)-ZnO, showed 8-fold higher photocatalytic activity in contrast to pristine ZnO. Tuning the doping content has been shown to have a significant impact on the sunlight-driven photocatalytic performance of ZnO, which can be attributed to their modulated optical properties and superior PL properties. Considering the fact that photocatalytic reactions are mainly controlled by the generated charge carriers on the catalyst surface, Mg doping was successfully employed to assist the generation of excess electrons, which leads to the enhanced photocatalytic reaction rate of the optimal photocatalyst. This study confirms the fact that optical response and textural properties are not the only influencing parameters for the improved performance of a photocatalyst. Doping induced charge carrier dynamics may also act as a significant factor for the superior photocatalytic performance.

Table 1. Physicochemical, Photocatalytic, and PEC Parameters of the Samples

	Physicochemical	Photocatalysis		PEC
Sample	Crystallite Size (nm)	Rate constant (min^{-1})	Photonic efficiency (%, 10^{-3})	Photocurrent (mA)
ZnO	15.04	0.003	1.56	0.14
Mg(0.5)-ZnO	17.70	0.005	1.78	0.17
Mg(1)-ZnO	22.06	0.009	1.90	0.48
Mg(3)-ZnO	17.70	0.025	6.21	1.54
Mg(5)-ZnO	18.30	0.017	5.33	0.73

Along with photocatalytic activity, the PEC water splitting performance of the as-prepared catalyst was also tested to showcase the dual application ability. The PEC performance of undoped and Mg-doped ZnO was investigated from the linear sweep voltammogram (LSV) using a three-electrode electrochemical workstation, as shown in Figure 4c. Similar to the photocatalytic test, samples showed an unchanged trend while analyzing their water splitting performance. LSV curves clearly demonstrate that ZnO showed a better photocurrent response after doping with Mg, thus indicating improved PEC water splitting performance. A photoanode composed of Mg(3)-ZnO showed a superior photocurrent response of 1.54 mA at 0.30 V vs Ag/AgCl in contrast with other electrodes. A broad oxidation peak was noticed for all the photoanodes, and as we increase the potential starting from 0 V (vs Ag/AgCl), Mg(3)-ZnO with optimal Mg content exhibits the highest oxidation current onset at 0.30 V, while the oxidation peak of other samples was centered around 0.50 to 0.60 V. The significant difference in onset potential and photocurrent response indicates the efficient generation and separation of charge carriers in Mg(3)-ZnO.[39,46] The reduction in the photocurrent value of other Mg-doped ZnO can be attributed to its poor optical properties as well as its high charge carrier recombination rate, as confirmed from the PL analyses. The optimally designed Mg(3)-ZnO with a high charge carrier lifetime (observed from the low PL emission intensity in Figure 4d) results in enhanced photocurrent response, which is nearly 11 times greater than the undoped ZnO. These findings clearly corroborate the role of precise doping in the ZnO lattice to increase the charge carrier density and their lifetime, which are highly desired for any catalytic or optoelectronic applications. These findings are in good agreement with those of Mallika et al., where they have shown the role of optimal Mg content in structural and optical properties of doped ZnO.[47]

DFT calculations were carried out to further understand the impact of the Mg dopant on the electronic structure of ZnO. Figure 5a shows the optimized structure of the ZnO lattice with an interstitial Mg atom. The wurtzite ZnO model is constructed by ZnO_4 tetrahedra stacked along the vertical direction, and the Mg dopant is placed in the lattice cavity to reduce the repulsive interactions. After optimizing the structure, the Mg atom spontaneously coordinates with the adjacent O atoms and forms an MgO_6 octahedral config-

https://doi.org/10.1021/acs.jpclett.3c00736
J. Phys. Chem. Lett. 2023, 14, 4134−4141

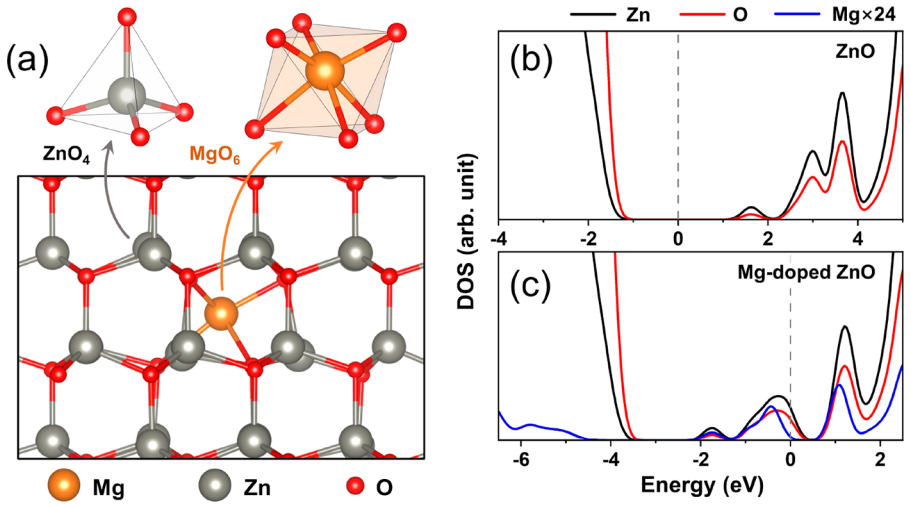

Figure 5. (a) Optimized structure of Mg-doped ZnO. The lattice is composed of ZnO_4 tetrahedra. The interstitial Mg atom forms an MgO_6 octahedron at the lattice cavity site. (b, c) Density of states (DOS) of pristine and Mg-doped ZnO. The dashed lines indicate the Fermi level. The Mg contribution to the DOS was magnified for comparison.

uration, which is consistent with the local structure of Mg^{2+} in rock salt MgO. The relevant density of states (DOS) of pristine and Mg-doped ZnO are plotted in Figure 5b,c. ZnO is a wide-bandgap semiconductor, while the Mg dopant acts as a donor contributing electrons in the conduction band. Moreover, the interaction between Mg and ZnO can stabilize these newly introduced electrons and lower their energy levels, generating shallow donor states in the forbidden band. These states are expected to provide additional carriers in photocatalytic and photoelectrochemical reactions and thus enhance the material performance. Both experimental and theoretical results claim that the contribution of Mg to the conduction band of ZnO leads to the enhanced performance of the doped material through extending the band separation (evident from the blue shift of the absorption edge) and reduced charge carrier recombination. The decrease (increase) in absorption edge (bandgap) and the generation of extra charge carriers are in good agreement with the optical and DFT analyses.

In summary, Mg-doped ZnO nanoflakes at different doping concentrations were prepared using the simple coprecipitation method. The photocatalytic and PEC performances of Mg-doped ZnO were evaluated and compared with undoped ZnO. The results illustrate that Mg(3)-ZnO (3 at. % Mg in ZnO) is the best composition for the photocatalytic contaminant degradation and PEC water splitting applications. The comparative experimental and DFT analyses were also carried out to extract insights into the role of doping on the optical and electronic properties of the modified material. The optical properties, studied by UV−vis and PL spectroscopies, change noticeably as the Mg content in ZnO increases. The optimal Mg-doped ZnO, which has 3 at. % Mg, exhibits a significant blue shift in the NBE peak and a reduced PL intensity compared with the other samples and has been found to exhibit high performance for the degradation of MB and photocurrent response in the water splitting test. The optimally designed Mg(3)-ZnO outperformed pristine ZnO by a factor of 8, while further increasing the Mg content reduced the performance significantly. Additionally, Mg(3)-ZnO exhibited a superior photocurrent response of 1.54 mA at the lowest onset potential, which is much higher than those of other Mg-ZnO samples. These outcomes highlight the role of the Mg doping content in improving the optical properties and hindering charge carrier recombination. Based on the optical analyses and DFT calculations, the modification in the absorption edge and the effective separation of charge carriers were assigned to the shift in the Fermi level and the formation of suitable dopant states. The results presented herein demonstrate that optimally designed Mg-doped ZnO nanoflakes can be an efficient material for solar-light-driven photocatalysis and PEC applications.

■ ASSOCIATED CONTENT

Supporting Information

The Supporting Information is available free of charge at https://pubs.acs.org/doi/10.1021/acs.jpclett.3c00736.

Details of the characterization techniques, photocatalytic experiment, and linear sweep voltammogram (LSV) experiment. Energy-dispersive X-ray spectroscopy (EDS) spectra of the samples and the corresponding element ratios (PDF)

■ AUTHOR INFORMATION

Corresponding Authors

Oleg V. Prezhdo − *Department of Chemistry and Department of Physics & Astronomy, University of Southern California, 90089 Los Angeles, California, United States;* orcid.org/0000-0002-5140-7500; Email: prezhdo@usc.edu

Ranjith G. Nair − *Solar Energy Materials Research & Testing Laboratory, Department of Physics, National Institute of Technology Silchar, 788010 Silchar, Assam, India;* Email: rgnair@phy.nits.ac.in

Authors

Abinash Das − *HSE University, 101000 Moscow, Russia*

Dongyu Liu − *HSE University, 101000 Moscow, Russia;* orcid.org/0000-0001-6941-1885

Riu Riu Wary − *Solar Energy Materials Research & Testing Laboratory, Department of Physics, National Institute of Technology Silchar, 788010 Silchar, Assam, India*

Andrey S. Vasenko − *HSE University, 101000 Moscow, Russia; I.E. Tamm Department of Theoretical Physics, P.N. Lebedev Physical Institute, Russian Academy of Sciences,*

https://doi.org/10.1021/acs.jpclett.3c00736
J. Phys. Chem. Lett. 2023, 14, 4134−4141

119991 Moscow, Russia; orcid.org/0000-0002-2978-8650

Complete contact information is available at: https://pubs.acs.org/10.1021/acs.jpclett.3c00736

Notes

The authors declare no competing financial interest.

■ ACKNOWLEDGMENTS

This research was supported in part through computational resources of HPC facilities at HSE University.[48] A.S.V. acknowledges support from the Basic Research Program of the HSE University. O.V.P. acknowledges funding of the U.S. National Science Foundation (CHE-2154367).

■ REFERENCES

(1) Su, J.; Wei, Y.; Vayssieres, L. Stability and Performance of Sulfide-, Nitride-, and Phosphide-Based Electrodes for Photocatalytic Solar Water Splitting. *J. Phys. Chem. Lett.* **2017**, *8*, 5228−5238.

(2) Zhang, W. X.; Yin, Y.; He, C. Spontaneous Enhanced Visible-Light-Driven Photocatalytic Water Splitting on Novel Type-II GaSe/CN and Ga_2SSe/CN vdW Heterostructures. *J. Phys. Chem. Lett.* **2021**, *12*, 5064−5075.

(3) Ahmed, T.; Edvinsson, T. Optical Quantum Confinement in Ultrasmall ZnO and the Effect of Size on Their Photocatalytic Activity. *J. Phys. Chem. C* **2020**, *124*, 6395−6404.

(4) Shi, R.; Fang, W.-H.; Vasenko, A. S.; Long, R.; Prezhdo, O. V. Efficient Passivation of DY Center in $CH_3NH_3PbBr_3$ by Chlorine: Quantum Molecular Dynamics. *Nano Res.* **2022**, *15*, 2112−2122.

(5) Ouyang, T.; Ye, Y. Q.; Tan, C.; Guo, S. T.; Huang, S.; Zhao, R.; Zhao, S.; Liu, Z. Q. 1D α-Fe_2O_3/ZnO Junction Arrays Modified by Bi as Photocathode: High Efficiency in Photoelectrochemical Reduction of CO_2 to HCOOH. *J. Phys. Chem. Lett.* **2022**, *13*, 6867−6874.

(6) Neppl, S.; Mahl, J.; Roth, F.; Mercurio, G.; Zeng, G.; Toma, F. M.; Huse, N.; Feulner, P.; Gessner, O. Nanoscale Confinement of Photo-Injected Electrons at Hybrid Interfaces. *J. Phys. Chem. Lett.* **2021**, *12*, 11951−11959.

(7) Kumar, P.; Kumar, A.; Rizvi, M. A.; Moosvi, S. K.; Krishnan, V.; Duvenhage, M. M.; Roos, W. D.; Swart, H. C. Surface, Optical and Photocatalytic Properties of Rb Doped ZnO Nanoparticles. *Appl. Surf. Sci.* **2020**, *514*, 145930.

(8) Zhang, N.; Chu, D.; Wang, L. One-step Synthesis of Novel Flower-like Sn-doped ZnO Architectures with Enhanced Photocatalytic Activity. *Surf. Interface Anal.* **2020**, *52*, 91−97.

(9) Yıldırım, Ö. A.; Unalan, H. E.; Durucan, C. Highly Efficient Room Temperature Synthesis of Silver-Doped Zinc Oxide (ZnO:Ag) Nanoparticles: Structural, Optical, and Photocatalytic Properties. *J. Am. Ceram. Soc.* **2013**, *96*, 766−773.

(10) Lv, F.; Liang, H.; Duan, Y. Superior Limit of Light-Absorption Improvement in Two-Dimensional Haeckelite GaN-ZnO by Nonadiabatic Molecular Dynamics Simulation. *J. Phys. Chem. Lett.* **2023**, *14*, 663−669.

(11) Wang, K.; Liu, D.; Liu, L.; Liu, J.; Hu, X. F.; Li, P.; Li, M.; Vasenko, A. S.; Xiao, C.; Ding, S. Tuning the local electronic structure of oxygen vacancies over copper-doped zinc oxide for efficient CO_2 electroreduction. *eScience* **2022**, *2*, 518−528.

(12) Chen, C.; Mei, W.; Yu, W.; Chen, X.; Zeng, L.; Tsang, Y.; Chao, Z.; Liu, X. Enhanced Sunlight-Driven Photocatalytic Property of Mg-Doped ZnO Nanocomposites with Three-Dimensional Graphene Oxide/MoS_2 Nanosheet Composites. *RSC Adv.* **2018**, *8*, 17399−17409.

(13) Ma, X.; Chu, W.; Wang, Y.; Li, Z.; Yang, J. Increasing the Efficiency of Photocatalytic Water Splitting via Introducing Intermediate Bands. *J. Phys. Chem. Lett.* **2023**, *14*, 779−784.

(14) Li, W.; She, Y.; Vasenko, A. S.; Prezhdo, O. V. Ab initio nonadiabatic molecular dynamics of charge carriers in metal halide perovskites. *Nanoscale* **2021**, *13*, 10239−10265.

(15) Rath, P. P.; Behera, S. S.; Priyadarshini, B.; Panda, S. R.; Mandal, D.; Sahoo, T.; Mishra, S.; Sahoo, T. R.; Parhi, P. K. Influence of Mg Doping on ZnO NPs for Enhanced Adsorption Activity of Congo Red Dye. *Appl. Surf. Sci.* **2019**, *491*, 256−266.

(16) Zheng, Y.; Cao, L.; Xing, G.; Bai, Z.; Huang, J.; Zhang, Z. Microscale Flower-like Magnesium Oxide for Highly Efficient Photocatalytic Degradation of Organic Dyes in Aqueous Solution. *RSC Adv.* **2019**, *9*, 7338−7348.

(17) Verma, D. K.; Kumar, B.; Kavita; Rastogi, R. B. Zinc Oxide- and Magnesium-Doped Zinc Oxide-Decorated Nanocomposites of Reduced Graphene Oxide as Friction and Wear Modifiers. *ACS Appl. Mater. Interfaces* **2019**, *11*, 2418−2430.

(18) Kara, R.; Mentar, L.; Azizi, A. Synthesis and Characterization of Mg-Doped ZnO Thin-Films Electrochemically Grown on FTO Substrates for Optoelectronic Applications. *RSC Adv.* **2020**, *10*, 40467−40479.

(19) Singh, J.; Kumar, P.; Hui, K. S.; Hui, K. N.; Ramam, K.; Tiwari, R. S.; Srivastava, O. N. Synthesis, Band-Gap Tuning, Structural and Optical Investigations of Mg Doped ZnO Nanowires. *CrystEngComm* **2012**, *14*, 5898.

(20) Giannozzi, P.; Baroni, S.; Bonini, N.; Calandra, M.; Car, R.; Cavazzoni, C.; Ceresoli, D.; Chiarotti, G. L.; Cococcioni, M.; Dabo, I.; Dal Corso, A.; de Gironcoli, S.; Fabris, S.; Fratesi, G.; Gebauer, R.; Gerstmann, U.; Gougoussis, C.; Kokalj, A.; Lazzeri, M.; Martin-Samos, L.; Marzari, N.; Mauri, F.; Mazzarello, R.; Paolini, S.; Pasquarello, A.; Paulatto, L.; Sbraccia, C.; Scandolo, S.; Sclauzero, G.; Seitsonen, A. P.; Smogunov, A.; Umari, P.; Wentzcovitch, R. M. QUANTUM ESPRESSO: a modular and open-source software project for quantum simulations of materials. *J. Phys.: Condens. Matter* **2009**, *21*, 395502.

(21) Giannozzi, P.; Andreussi, O.; Brumme, T.; Bunau, O.; Buongiorno Nardelli, M.; Calandra, M.; Car, R.; Cavazzoni, C.; Ceresoli, D.; Cococcioni, M.; Colonna, N.; Carnimeo, I.; Dal Corso, A.; de Gironcoli, S.; Delugas, P.; DiStasio, R. A.; Ferretti, A.; Floris, A.; Fratesi, G.; Fugallo, G.; Gebauer, R.; Gerstmann, U.; Giustino, F.; Gorni, T.; Jia, J.; Kawamura, M.; Ko, H. Y.; Kokalj, A.; Küçükbenli, E.; Lazzeri, M.; Marsili, M.; Marzari, N.; Mauri, F.; Nguyen, N. L.; Nguyen, H. V.; Otero-de-la-Roza, A.; Paulatto, L.; Poncé, S.; Rocca, D.; Sabatini, R.; Santra, B.; Schlipf, M.; Seitsonen, A. P.; Smogunov, A.; Timrov, I.; Thonhauser, T.; Umari, P.; Vast, N.; Wu, X.; Baroni, S. Advanced capabilities for materials modelling with Quantum ESPRESSO. *J. Phys.: Condens. Matter* **2017**, *29*, 465901.

(22) Perdew, J. P.; Burke, K.; Ernzerhof, M. Generalized Gradient Approximation Made Simple. *Phys. Rev. Lett.* **1996**, *77*, 3865−3868.

(23) Perdew, J. P.; Ernzerhof, M.; Burke, K. Rationale for mixing exact exchange with density functional approximations. *J. Chem. Phys.* **1996**, *105*, 9982−9985.

(24) van Setten, M. J.; Giantomassi, M.; Bousquet, E.; Verstraete, M. J.; Hamann, D. R.; Gonze, X.; Rignanese, G. M. The PseudoDojo: Training and grading a 85 element optimized norm-conserving pseudopotential table. *Comput. Phys. Commun.* **2018**, *226*, 39−54.

(25) Momma, K.; Izumi, F. VESTA 3 for three-dimensional visualization of crystal, volumetric and morphology data. *J. Appl. Crystallogr.* **2011**, *44*, 1272−1276.

(26) Haja Hameed, A. S.; Karthikeyan, C.; Sasikumar, S.; Senthil Kumar, V.; Kumaresan, S.; Ravi, G. Impact of Alkaline Metal Ions Mg^{2+}, Ca^{2+}, Sr^{2+} and Ba^{2+} on the Structural, Optical, Thermal and Antibacterial Properties of ZnO Nanoparticles Prepared by the Co-Precipitation Method. *J. Mater. Chem. B* **2013**, *1*, 5950.

(27) Etacheri, V.; Roshan, R.; Kumar, V. Mg-Doped ZnO Nanoparticles for Efficient Sunlight-Driven Photocatalysis. *ACS Appl. Mater. Interfaces* **2012**, *4*, 2717−2725.

(28) Aykut, Y.; Parsons, G. N.; Pourdeyhimi, B.; Khan, S. A. Synthesis of Mixed Ceramic $Mg_xZn_{1-x}O$ Nanofibers via Mg^{2+} Doping Using Sol−Gel Electrospinning. *Langmuir* **2013**, *29*, 4159−4166.

(29) Saloga, P. E. J.; Thünemann, A. F. Microwave-Assisted Synthesis of Ultrasmall Zinc Oxide Nanoparticles. *Langmuir* **2019**, *35*, 12469−12482.

(30) Yang, J.; Wang, Y.; Kong, J.; Yu, M.; Jin, H. Synthesis of Mg-Doped Hierarchical ZnO Nanostructures via Hydrothermal Method and Their Optical Properties. *J. Alloys Compd.* **2016**, *657*, 261−267.
(31) Ding, Y.; Gao, P. X.; Wang, Z. L. Catalyst−Nanostructure Interfacial Lattice Mismatch in Determining the Shape of VLS Grown Nanowires and Nanobelts: A Case of Sn/ZnO. *J. Am. Chem. Soc.* **2004**, *126*, 2066−2072.
(32) Liu, Y.; Huang, D.; Liu, H.; Li, T.; Wang, J. ZnO Tetrakaidecahedrons with Coexposed {001}, {101}, and {100} Facets: Shape-Selective Synthesis and Enhancing Photocatalytic Performance. *Cryst. Growth Des.* **2019**, *19*, 2758−2764.
(33) Sabbaghan, M.; Anaraki Firooz, A.; Jan Ahmadi, V. The Effect of Template on Morphology, Optical and Photocatalytic Properties of ZnO Nanostructures. *J. Mol. Liq.* **2012**, *175*, 135−140.
(34) Kaushal, A.; Kaur, D. Effect of Mg Content on Structural, Electrical and Optical Properties of $Zn_{1-x}Mg_xO$ Nanocomposite Thin Films. *Sol. Energy Mater. Sol. Cells* **2009**, *93*, 193−198.
(35) Adam, R. E.; Alnoor, H.; Pozina, G.; Liu, X.; Willander, M.; Nur, O. Synthesis of Mg-Doped ZnO NPs via a Chemical Low-Temperature Method and Investigation of the Efficient Photocatalytic Activity for the Degradation of Dyes under Solar Light. *Solid State Sci.* **2020**, *99*, 106053.
(36) Misra, M.; Kapur, P.; Singla, M. L. Surface Plasmon Quenched of near Band Edge Emission and Enhanced Visible Photocatalytic Activity of Au@ZnO Core-Shell Nanostructure. *Appl. Catal. B: Environ.* **2014**, *150−151*, 605−611.
(37) Goktas, A.; Tumbul, A.; Aba, Z.; Durgun, M. Mg Doping Levels and Annealing Temperature Induced Structural, Optical and Electrical Properties of Highly c-Axis Oriented ZnO:Mg Thin Films and Al/ZnO:Mg/p-Si/Al Heterojunction Diode. *Thin Solid Films* **2019**, *680*, 20−30.
(38) Shan, F. K.; Kim, B. I.; Liu, G. X.; Liu, Z. F.; Sohn, J. Y.; Lee, W. J.; Shin, B. C.; Yu, Y. S. Blueshift of near Band Edge Emission in Mg Doped ZnO Thin Films and Aging. *J. Appl. Phys.* **2004**, *95*, 4772−4776.
(39) Sahoo, P.; Sharma, A.; Padhan, S.; Thangavel, R. Visible Light Driven Photosplitting of Water Using One Dimensional Mg Doped ZnO Nanorod Arrays. *Int. J. Hydrog. Energy* **2020**, *45*, 22576−22588.
(40) Makino, T.; Tuan, N. T.; Sun, H. D.; Chia, C. H.; Segawa, Y.; Kawasaki, M.; Ohtomo, A.; Tamura, K.; Suemoto, T.; Akiyama, H.; Baba, M.; Saito, S.; Tomita, T.; Koinuma, H. Temperature Dependence of near Ultraviolet Photoluminescence in ZnO/(Mg, Zn)O Multiple Quantum Wells. *Appl. Phys. Lett.* **2001**, *78*, 1979−1981.
(41) Guo, M. Y.; Ng, A. M. C.; Liu, F.; Djurišić, A. B.; Chan, W. K.; Su, H.; Wong, K. S. Effect of Native Defects on Photocatalytic Properties of ZnO. *J. Phys. Chem. C* **2011**, *115*, 11095−11101.
(42) Das, A.; Mathan Kumar, P.; Bhagavathiachari, M.; Nair, R. G. Shape Selective Flower-like ZnO Nanostructures Prepared via Structure-Directing Reagent Free Methods for Efficient Photocatalytic Performance. *Mater. Sci. Eng., B* **2021**, *269*, 115149.
(43) Sambandam, B.; Michael, R. J. V.; Manoharan, P. T. Oxygen Vacancies and Intense Luminescence in Manganese Assisted ZnO Microflowers for Visible Light Water Splitting. *Nanoscale* **2015**, *7*, 13935−13942.
(44) Jiang, J.; Mu, Z.; Xing, H.; Wu, Q.; Yue, X.; Lin, Y. Insights into the Synergetic Effect for Enhanced UV/Visible-Light Activated Photodegradation Activity via Cu-ZnO Photocatalyst. *Appl. Surf. Sci.* **2019**, *478*, 1037−1045.
(45) Cardenas-Morcoso, D.; Gualdrón-Reyes, A. F.; Ferreira Vitoreti, A. B.; García-Tecedor, M.; Yoon, S. J.; Solis de la Fuente, M.; Mora-Seró, I.; Gimenez, S. Photocatalytic and Photoelectrochemical Degradation of Organic Compounds with All-Inorganic Metal Halide Perovskite Quantum Dots. *J. Phys. Chem. Lett.* **2019**, *10*, 630−636.
(46) Hsu, Y.-K.; Chen, Y.-C.; Lin, Y.-G. Novel ZnO/Fe_2O_3 Core−Shell Nanowires for Photoelectrochemical Water Splitting. *ACS Appl. Mater. Interfaces* **2015**, *7*, 14157−14162.
(47) Mallika, A.N.; Ramachandra Reddy, A.; Sowri Babu, K.; Sujatha, C.; Venugopal Reddy, K. Structural and photoluminescence properties of Mg substituted ZnO nanoparticles. *Opt. Mater.* **2014**, *36*, 879−884.
(48) Kostenetskiy, P. S.; Chulkevich, R. A.; Kozyrev, V. I. HPC Resources of the Higher School of Economics. *J. Phys. Conf. Ser.* **2021**, *1740*, 012050.

https://doi.org/10.1021/acs.jpclett.3c00736
J. Phys. Chem. Lett. 2023, 14, 4134−4141